

1 Real Time 3D Observations of Portland Cement Carbonation at CO₂ 2 Storage Conditions

3 Elvia A. Chavez Panduro,* Benoît Cordonnier, Kamila Gawel, Ingrid Børve, Jaisree Iyer, Susan A. Carroll,
4 Leander Michels, Melania Rogowska, Jessica Ann McBeck, Henning Osholm Sørensen,
5 Stuart D. C. Walsh, François Renard, Alain Gibaud, Malin Torsæter, and Dag W. Breiby*



Cite This: <https://dx.doi.org/10.1021/acs.est.0c00578>



Read Online

ACCESS |



Metrics & More

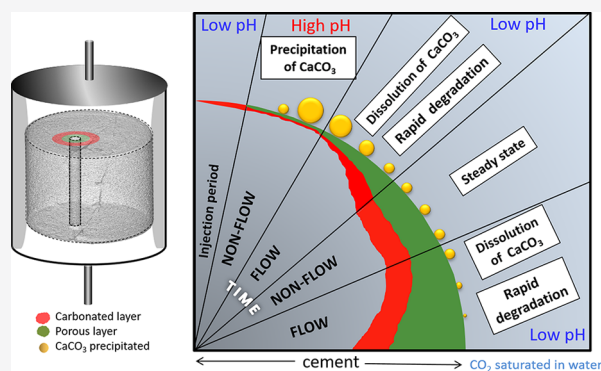


Article Recommendations



Supporting Information

6 **ABSTRACT:** Depleted oil reservoirs are considered a viable solution
7 to the global challenge of CO₂ storage. A key concern is whether the
8 wells can be suitably sealed with cement to hinder the escape of CO₂.
9 Under reservoir conditions, CO₂ is in its supercritical state, and the high
10 pressures and temperatures involved make real-time microscopic
11 observations of cement degradation experimentally challenging. Here,
12 we present an in situ 3D dynamic X-ray micro computed tomography
13 (μ -CT) study of well cement carbonation at realistic reservoir stress,
14 pore-pressure, and temperature conditions. The high-resolution time-
15 lapse 3D images allow monitoring the progress of reaction fronts in
16 Portland cement, including density changes, sample deformation, and
17 mineral precipitation and dissolution. By switching between flow and
18 nonflow conditions of CO₂-saturated water through cement, we were
19 able to delineate regimes dominated by calcium carbonate precipitation
20 and dissolution. For the first time, we demonstrate experimentally the impact of the flow history on CO₂ leakage risk for cement
21 plugging. In-situ μ -CT experiments combined with geochemical modeling provide unique insight into the interactions between CO₂
22 and cement, potentially helping in assessing the risks of CO₂ storage in geological reservoirs.



23 ■ INTRODUCTION

24 Finding a solution to the global CO₂ emissions problem has
25 become increasingly important in recent years.¹ One of the
26 most promising mitigating measures is its sequestration in
27 depleted oil and gas reservoirs,² using cement to seal the
28 wellbores. However, the risk of CO₂ leakage to the atmosphere
29 has hindered large scale implementation. According to the
30 Intergovernmental Panel on Climate Change (IPCC), leakage
31 along wellbores imposes the largest risk of CO₂ migration
32 toward the surface.² These leakage pathways can exist both in
33 the cement plug or in the annular region between the casing
34 and the caprock and can be formed during drilling, completion,
35 or abandonment.³ One potential problem is that the sealing
36 properties of the cement will be affected when the CO₂ reacts
37 with cement along the pre-existing leakage paths. To assess the
38 risk related to CO₂ sequestration in depleted oil and gas
39 reservoirs, an enhanced understanding of the influence of CO₂
40 on Portland cement under reservoir conditions is critical.

41 When CO₂ saturated water is in contact with cement at
42 reservoir conditions, a series of thoroughly investigated
43 chemical reactions lead to cement carbonation.^{4,5} Three
44 distinct reaction zones form in cement upon carbonation and
45 propagate away from the cement/carbonated-water interface
46 with time.^{4,6} The first stage of carbonation involves dissolution

of portlandite (Ca(OH)₂, CH in cement chemistry notation) 47
to form a portlandite depleted zone. In the second stage, a 48
carbonated zone forms by the precipitation of dissolved 49
portlandite as calcium carbonate (CaCO₃, C \bar{C}) upon reaction 50
with carbonic acid. The last stage of carbonation is the 51
dissolution of this newly formed C \bar{C} through a bicarbonation 52
process producing an amorphous porous silica zone.^{4,7-12} The 53
carbonation rate in cement depends on the chemical 54
(portlandite content, calcium silicate hydrate content) and 55
physical properties of cement (porosity, tortuosity) as well as 56
the processing conditions (curing time, temperature, pressure, 57
and fluid flow rate).¹³⁻¹⁶ 58

It has been observed that fractures present in cement can 59
either close (self-seal) or open upon carbonation. Self-sealing is 60
usually caused by precipitation of C \bar{C} ^{17,18} but may also be a 61
result of cement swelling¹⁰ or cement deformation,¹⁹ whereas 62
fracture opening is typically caused by the dissolution of 63

Received: January 29, 2020

Revised: June 6, 2020

Accepted: June 11, 2020

Published: June 11, 2020

64 cement compounds²⁰ and/or stresses induced by crystal
65 precipitation.²¹ Several studies attempting to explain the
66 sealing behavior of fractures have emphasized the importance
67 of flow rate, either in terms of Darcy flux²² or residence
68 time.^{12,19,23} In connected fractures running parallel to the
69 wellbore, the CO₂ fluid can reach high flow rates driven by
70 pressure gradients.^{24,25} Newell et al. stated that the potential
71 leakage rates calculated from a natural CO₂ producer with a
72 wellbore permeability between 1 and 10 mD (inferred over a
73 single 3 m interval) are around 0.3–3 mL/h.²⁴ Laboratory
74 experiments on samples subjected to flow of CO₂-fluids are
75 typically in the range of 1–100 mL/h.^{6,10,12,26} Wolterbeek et
76 al. stated that the flow rate can vary considerably with time and
77 even display pulsed or periodic flow behavior.²⁷ Field studies
78 report that the occurrence of periodic flow include Taylor-
79 bubble formation, competition between capillary and buoyancy
80 effects, and pressure driven aperture.^{28–31} Thus, more work is
81 needed to quantitatively understand the impact of flow history
82 on the sealing behavior of fractures, as in real CO₂ storage
83 sites, the reservoir pressures driving leakage are expected to
84 change over time.

85 Owing to its complexity, only few field studies have
86 characterized CO₂ well integrity. Carey et al. studied Portland
87 cement retrieved from an enhanced oil recovery (EOR)
88 reservoir at the SACROC unit in Texas.³² Crow et al. studied
89 cement from a natural CO₂ reservoir in the Dakota sandstone
90 formation.³³ In both studies, even if the cement was altered
91 due to CO₂ exposure, it was concluded that the cement could
92 still provide an effective barrier to CO₂ migration. Ex-situ static
93 and flow-through laboratory experiments that aim to under-
94 stand the carbonation processes in cement have several
95 limitations. An understanding of the dynamics of the
96 carbonation processes in such experiments is difficult to obtain
97 because it is challenging to decouple the effects of carbonation
98 from the effects of depressurization prior to observing the
99 sample.²⁶ We have recently reported kinetics of carbonation of
100 Portland cement based on an in situ X-ray computed
101 tomography experiment; however, due to (flux) limitations
102 of the in-house X-ray tomography setup, the sample cell had to
103 be kept relatively thin and transparent, thus preventing the use
104 of realistic stress and fluid pressure conditions.³⁴

105 Here, in an effort to directly observe the cement carbonation
106 at relevant reservoir conditions, i.e., representative axial and
107 radial confining stresses as well as high pore pressure and
108 temperature, we report in situ microtomography (μ -CT)
109 experiments using a unique X-ray tomography-compatible
110 triaxial deformation apparatus (HADES).³⁵ We observed, in
111 3D and real-time, cement reaction fronts propagating through
112 the cement sample as well as precipitation and dissolution of
113 CaCO₃ in leakage paths present in the cement exposed to
114 varying CO₂ saturated-water flow conditions. The experiment
115 thus provided unique data that can be used for refining
116 geomechanical and geochemical numerical models on the
117 cement carbonation and self-sealing processes.

118 ■ MATERIALS AND METHODS

119 **Sample Preparation.** Class G cement (High Sulfate
120 Resistant Well Cement, Norcem AS) was mixed according to
121 an API recommended practice³⁶ with a water/cement mass
122 ratio of 0.44. The slurry was poured into a cylindrical plastic
123 mold with a diameter of 5 mm and a length of 4 mm. A
124 smooth cylindrical channel running through the sample was
125 artificially made by having a nylon fishing line (diameter 0.4

mm) in the cement slurry during curing. The total curing time
126 was about 2 weeks. Additionally, for comparisons of reaction
127 behavior, a rougher “natural” fracture, also extending through
128 the sample length, was purposely introduced by gently cleaving
129 the specimen with a scalpel immediately prior to the
130 experiment. The resulting two pieces were snugly fit back
131 together inside the confining rubber gasket. See SI S1 for
132 details. 133

Experimental Setup. The cement sample was measured
134 using the HADES triaxial deformation apparatus.³⁵ The sample
135 equipment comprises the cell itself, two pumps that control the
136 confining and axial pressure, and two injection pumps that
137 control the fluid pressure (Figure S1); see Renard et al.³⁵ The
138 cement sample was placed inside a rubber gasket, together with
139 two sandstone spacers (7% porosity, 5 mm diameter, 3 mm
140 length) above and below to achieve a homogeneous flow of
141 CO₂. The CO₂-saturated water was pressurized to 28 MPa.
142 The CO₂-saturated fluid was injected axially into the cement
143 sample from the top. The working fluid pressure and
144 temperature were 28 MPa and 80 °C. The cement sample
145 was kept under realistic axial and radial confining pressures of
146 31 and 30 MPa, respectively. During the experiment, different
147 CO₂ flow regimes ranging from hydrostatic (stagnant) to
148 purging were imposed to test the dependence of flow history
149 on the reaction kinetics, cf. Figure 1b and SI S1. 150 ft

Synchrotron Measurement. X-ray tomography data were
151 acquired at the ESRF ID19 beamline, using a high photon
152 energy of 84 keV to enable the X-ray radiation to be
153 transmitted through the titanium walls of the deformation
154 apparatus. The sample–detector distance was 1200 mm, giving
155 edge-enhanced phase contrast.³⁷ 2D projections were obtained
156 with a PCO Dimax detector with a pixel size of 6.45 μ m and an
157 exposure time of 0.05 s. For each time step, a full μ -CT data set
158 consisting of 2000 radiographs (projections) over 180° were
159 acquired. In total, 103 time-steps (full tomograms) were
160 recorded over a period of nearly 20 h. The data were
161 reconstructed using PyHST2³⁸ involving filtered back-projec-
162 tion coupled with the phase contrast algorithm.³⁷ Three-
163 dimensional image analysis was done using ImageJ; see more
164 details in SI S3. 165

Geochemical Model. Chemical reaction calculations in an
166 idealized 2D geometry were performed to relate the
167 experimental observations to solution chemistry. In the
168 absence of experimental data on ion concentrations, pH, and
169 saturation indices of the minerals, the model predictions
170 provide information that allows us to corroborate our
171 hypotheses explaining the experimental observations. The
172 experimentally calibrated model (calibrated to a different set of
173 experimental observations)^{19,39} couples flow of carbonated
174 water through fractures at cement–cement/cement–caprock
175 interfaces, advective and diffusive transport of the dissolved
176 chemical species along the fracture, diffusive transport of the
177 chemical species within the cement, and geochemical reactions
178 between the cement and carbonated water. The model can
179 predict calcite precipitation in a fracture but is limited to
180 predicting uniform precipitation instead of precipitation at
181 specific nucleation sites. In addition, the model assumes that
182 once calcite precipitates at a fracture surface, it passivates the
183 surface and prevents the growth of the porous amorphous
184 silicate layer until the surface precipitate is completely
185 dissolved. A detailed description of the model can be found
186 in SI S5 and other references.^{16,19,39} 187

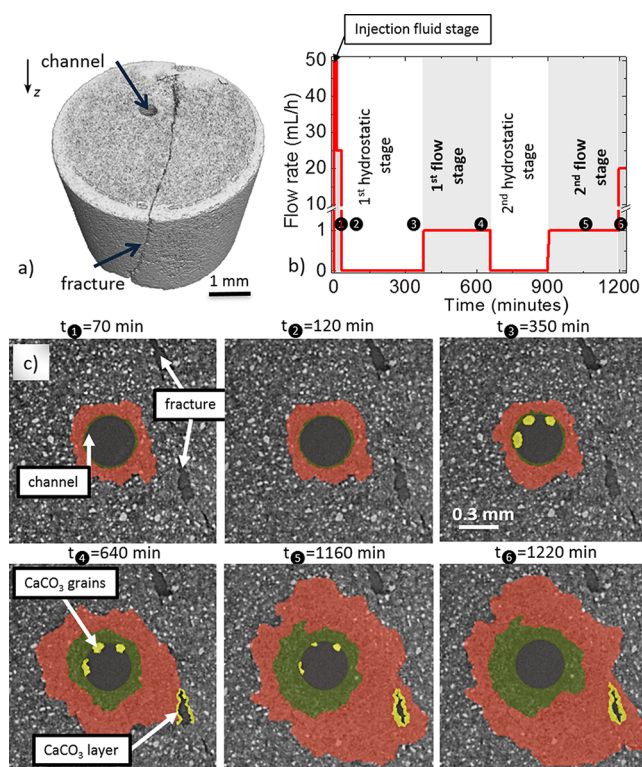


Figure 1. Overview of the in situ μ -CT experiment of carbonation of Portland cement in the presence of CO_2 . (a) Perspective 3D view of the Portland cement sample, with the channel and the fracture indicated by arrows. (b) The flow history of CO_2 saturated water through the sample during the experiment. (c) Lateral μ -CT cross-sections at $z = 2$ mm showing the region near the channel, obtained at the indicated times. The images show the evolution of the carbonated zone (red) and porous silica zone (green) in the cement, and precipitation/dissolution of calcium carbonate (yellow) in the channel and the fracture. The raw images without the color segmentation are provided in Figure S11.

188 Geomechanical Calculation. Digital volume correlation
 189 (DVC) analysis was performed to extract the evolution of the
 190 displacement field within the sample, using the software
 191 Tomowarp2;⁴⁰ see also refs 41 and 42. DVC analysis cross-
 192 correlates voxel intensities in series of tomograms in order to
 193 derive the displacement field as a function of time. For these
 194 experiments, we used a 10-voxel node spacing, averaging the
 195 displacement field over subvolumes of 10^3 voxels, in a central
 196 region of the sample centered around the channel. From DVC
 197 analysis of the whole sample, it can be seen (cf. SI) that the
 198 whole sample tilted slightly. Consequently, after removing
 199 sporadic unphysically large outlier values from the displace-
 200 ment field, the averaged lateral displacements (locally
 201 corresponding to trivial sample translation) were subtracted
 202 before the lateral displacement field was plotted superposed on
 203 slices from the tomography data.

204 ■ RESULTS AND DISCUSSION

205 Overview of Experimental Observations. The cylin-
 206 drical Portland cement sample was produced with both a
 207 smooth “artificial” cylindrical inner channel (diameter ~ 0.4
 208 mm) and a rough “natural” fracture around ~ 0.5 mm away
 209 from the channel, both extending through the full length of the
 210 sample (Figure 1a). The specimen was designed to maximize
 211 the amount of information that could be retrieved during the

limited duration of synchrotron access. The cement was 212
 exposed to the pressure (28 MPa) and temperature (80 °C) 213
 conditions corresponding to a ~ 2 km depth in a depleted oil 214
 reservoir.⁴³ Alternating flow and hydrostatic (nonflow) 215
 conditions of CO_2 saturated water were imposed on the 216
 sample to delineate precipitation versus dissolution-dominated 217
 regimes (SI Note 1 and Figure 1b). Water was chosen instead 218
 of the 0.5 M NaCl brine commonly used in order to increase 219
 the CO_2 saturation and hence the reaction rates. The cement 220
 specimen was monitored with synchrotron X-ray μ -CT, 221
 enabling the 3D morphological impact of the chemical 222
 reactions (Figure 1c) to be followed in time. We observed 223
 the progression of the reaction zones in the cement, the 224
 competing precipitation vs dissolution dynamics of CaCO_3 225
 observed in both the channel and the fracture upon exposure 226
 to CO_2 , and the concomitant mechanical specimen deforma- 227
 tion. When the sample was subjected to the confining and axial 228
 pressures at the beginning of the experiment, most of the 229
 cavities in the natural fracture were closed, thus reducing the 230
 fracture aperture. CaCO_3 precipitation was observed at the ends of 231
 the fracture (cf. Figures 2 and 4). Therefore, the CaCO_3 deposits 232

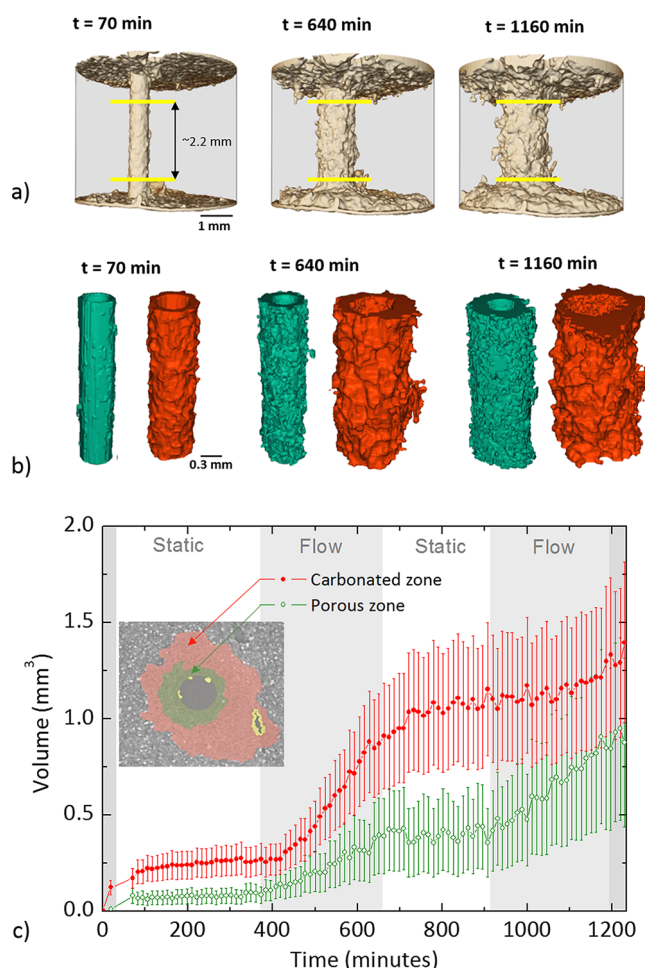


Figure 2. Reaction fronts in the cement as a function of time retrieved from μ -CT analysis. (a) 3D volume rendering of the whole specimen, showing reacted cement in yellow, at 70, 640, and 1160 min, (b) 3D rendering of carbonated (red) and porous silica zones (green), and (c) volume evolution of the reacted zones within the middle part of the sample, as delineated with yellow lines in part a. The inset shows a segmented cross-section sample.

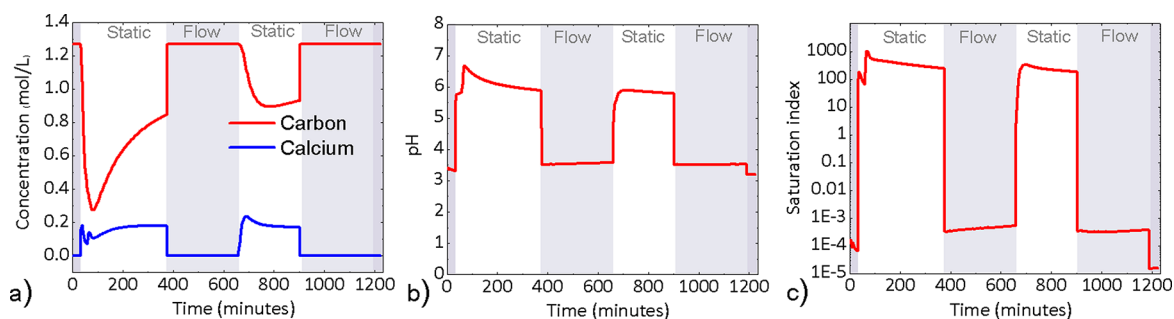


Figure 3. Numerical geochemical model predictions. (a) Calcium and carbon concentrations, (b) pH, and (c) saturation index of calcite at the outlet face of the sample as a function of time.

233 and the confining stress applied to the sample prevented fluid
234 transport in the fracture, so essentially all the flowing fluid was
235 forced to go through the channel. Interestingly, both in the
236 channel and the fracture, precipitation of CC was observed, but
237 their respective precipitation processes were different.

238 **Cement Carbonation and Reaction Zones Propagation.**
239 During the experiment, changes in the density of cement
240 were observed at all the surfaces that were in contact with
241 CO_2 -saturated water, i.e., at both ends of the cement cylinder
242 and around the channel; see Figure 2. The mass density of the
243 carbonated zone increased compared to the unreacted cement
244 due to the abundance of CC .¹¹ Calcium carbonate has higher
245 density compared to the calcium hydroxide present in the
246 unreacted cement, thus increasing the attenuation, which is
247 observed in the μ -CT images as brighter gray scale levels.
248 When the carbonated zone progresses into the cement sample,
249 the amorphous porous silica zone develops in between the
250 carbonated layer and the cement surface (Figure 1), giving a
251 decrease in the X-ray attenuation; see also SI S2. The
252 carbonated zone and the porous silica zone were clearly
253 discernible in the reconstructed cross-section images, including
254 how they propagated over time (Figure 1c, S11). The
255 portlandite depleted zone predicted by several previous studies
256 could arguably be observed in the μ -CT images as a slightly
257 less dense region with a thickness of $\sim 20 \mu\text{m}$ outside the
258 carbonated zone (SI S4). As shown by the model predictions
259 in SI S3, the thickness of the different layers depends on the
260 composition of the unreacted cement, with higher portlandite
261 content in the cement resulting in thinner reacted layers.¹⁶

262 The temporal evolution of the volumes of the carbonated
263 and porous silica zones (Figure 2 and S14) shows that the
264 growth rates of the carbonated and porous silica regions were
265 significant under flow conditions while they were small and
266 negligible under hydrostatic conditions. The volumetric
267 growth rates of the carbonated and porous silica regions
268 were found to be $2.5 \times 10^{-3} \pm 8 \times 10^{-5}$ and $1 \times 10^{-3} \pm 5 \times$
269 $10^{-5} \text{ mm}^3/\text{min}$ for the first flow phase and $7.0 \times 10^{-4} \pm 1.1 \times$
270 10^{-4} and $1.8 \times 10^{-3} \pm 8 \times 10^{-5} \text{ mm}^3/\text{min}$ for the second flow
271 phase, consistent with previous reports of cement alteration
272 slowing with time.^{14,19} This slowdown arises from a change in
273 the properties of the cement during the course of experiment,
274 in particular, the growth of the dense carbonated zone^{14,44} with
275 low permeability that hinders the transport of reactants into
276 the unreacted cement. In addition, the distance of diffusion of
277 the reactants from the channel to the unreacted cement
278 increases with time, which also contributes to slowing down
279 the carbonation processes. We note also that while in the first
280 flow phase, the growth rate of the carbonated layer was higher
281 than the rate of the porous silica layer, in the second flow

282 phase, the porous silica layer grew faster than the carbonated
283 layer.

284 The results confirm that the rate of cement alteration
285 depends on the CO_2 flow conditions, with rapid cement
286 degradation under flow conditions^{5,44,45} and slow degradation
287 for hydrostatic conditions.^{4,6} The flow rate controls the CO_2 -
288 saturated water composition (calcium and carbonate content,
289 pH) in the channel and determines the rate of cement
290 degradation because diffusive transport of reactants into the
291 cement is proportional to their concentration gradients. During
292 the hydrostatic stages, the concentration gradient of the
293 reactants is smaller due to the reactant consumption and the
294 accumulation of products in the channel fluid.

295 The geochemical modeling results are given in Figure 3,
296 giving predictions of the temporal evolution of the total
297 calcium (i.e., aqueous Ca^{2+} , CaHCO_3^+ , CaCO_3) and total
298 carbon concentrations (i.e., aqueous CaHCO_3^+ , CaCO_3 , CO_2 ,
299 H_2CO_3 , HCO_3^- , CO_3^{2-}) at the outlet face of the sample. In
300 the convective stages, the effluent carbon content is expected
301 to be almost equal to the inlet concentrations. The modeling
302 supports that the carbon content at the outlet in the second
303 hydrostatic stage is higher than that in the first one, implying
304 that less carbon is consumed in the reaction with the cement
305 during the second hydrostatic phase.

306 The porous silica zone grew during the flow stages and did
307 not propagate during the hydrostatic stages. The conditions
308 that promote CC dissolution and propagation of the porous
309 silica zone are low pH and undersaturation of the surrounding
310 solution with respect to CC .⁴⁶ During flow conditions, the pH
311 in the channel is expectedly low (cf. Figure 3) due to the
312 constant supply of carbonic acid and the washing away of the
313 calcium ions, which keeps the water undersaturated and
314 promotes dissolution of CC . In the hydrostatic stages, the
315 model results support the intuition that the pH increases and
316 saturation with respect to calcite is rapidly reached in the
317 channel (within less than 3 min), which prevents further
318 dissolution of the CC in the cement and thus effectively arrests
319 the growth of the porous silica zone. The growth of the porous
320 silica zone is probably reaction rate-limited rather than
321 transport-limited because the porous permeable layer is not
322 expected to hinder diffusion of the reactants in the same way
323 that the carbonated layer does.⁴⁴ Nevertheless, we observe
324 differences in the propagation rate of the porous silica zone in
325 both flow stages. The volumetric growth of the porous silica
326 layer during the second flow stage was faster than that in the
327 first flow stage, perhaps because of the progressively increasing
328 surface area from which it is dissolved as the porous silica zone
329 grows.

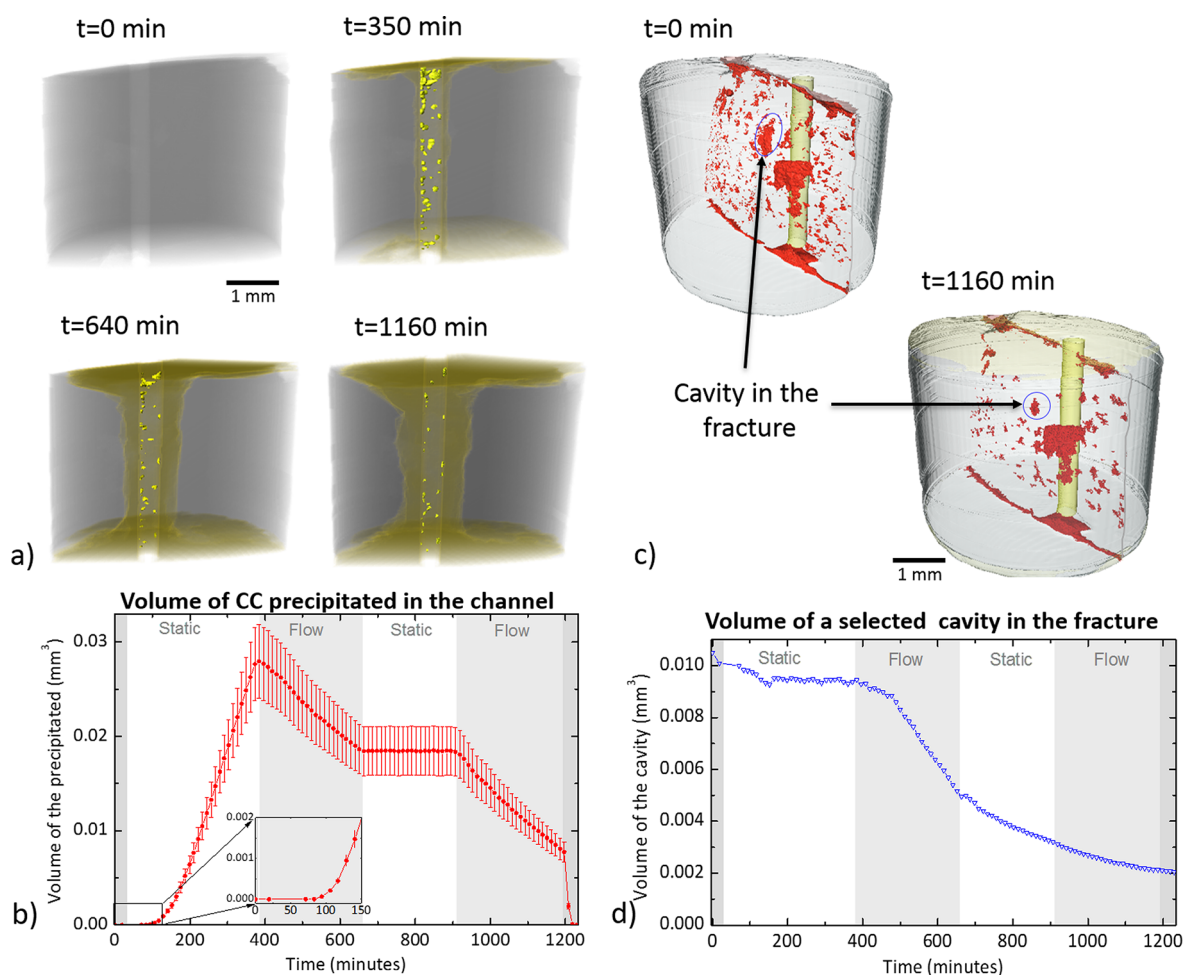


Figure 4. Precipitation in the channel and the fracture. (a) 3D visualization of precipitated CaCO_3 in the channel, the crystals are highlighted in sharp yellow, reacted cement in yellow-brown and the unreacted cement cylinder is in semitransparent gray. (b) Time evolution of the precipitated CaCO_3 volume in the channel. The inset shows a zoomed-in view of the first 150 min (c) 3D visualization of the fracture (in red) before and after CO_2 exposure. The channel is represented in transparent yellow. (d) Time evolution of the volume of the selected cavity in the fracture shown in part c.

330 **Precipitation of CaCO_3 in the Channel.** During the first
 331 hydrostatic phase, CC crystals precipitated onto the walls of
 332 the smooth cylindrical channel. Figure 4 shows the temporal
 333 evolution of the precipitated CaCO_3 volume. During the first
 334 90 min, no precipitation in the channel was observed. The total
 335 volume of CC precipitated in the channel grew almost linearly
 336 between $t = 150$ and 370 min with a growth rate of 1.2×10^{-4}
 337 $\pm 10^{-6} \text{ mm}^3/\text{min}$. The precipitation was first observed at the
 338 top of the channel, close to the CO_2 -saturated water inlet,
 339 which suggests a concentration gradient along the channel, cf.
 340 Figure S15. Similarly, it is likely that the CO_2 -fluid exposure to
 341 the end surface of the cement specimen (cf. Figure 2a) may
 342 have slightly preconditioned the fluid (reduced the concen-
 343 tration of carbonic acid) before entering the channel. As soon
 344 as the flow was introduced, the precipitates in the channel
 345 started to dissolve at a rate of $3.6 \times 10^{-5} \pm 5 \times 10^{-7} \text{ mm}^3/\text{min}$.
 346 When the flow was paused after $t = 650$ min, the dissolution
 347 also stopped, and no crystal growth was observed during the
 348 second hydrostatic stage. At $t = 900$ min, the flow was re-
 349 established, resulting in resumed dissolution of CC . Further
 350 increase in the flow rate from 1 to 20 mL/h toward the end of
 351 the experiment resulted in a ten times higher dissolution rate,
 352 completely emptying the cylindrical channel of solid CaCO_3 .

At the temperature and pressure conditions used in the 353
 experiment, calcium carbonate should have precipitated in the 354
 channel in the form of aragonite.⁴⁷ However, the shape of the 355
 growing crystals was nearly spherical, suggesting that the 356
 polymorph formed could be vaterite.^{48,49} The model 357
 prediction of a pH between 6 and 7 in the channel (Figure 3b) 358
 during the static phase further supports the hypothesis that 359
 the polymorphic form of the precipitated CC could be 360
 vaterite.⁵⁰ Due to the complexity of the CC precipitation 361
 process, other techniques will be needed to conclude about the 362
 exact nature of this polymorph. 363

Precipitation of CC requires oversaturation of the water with 364
 CC . The saturation index of calcite plotted in Figure 3 is 365
 defined as $[a_{\text{Ca}^{2+}}][a_{\text{CO}_3^{2-}}]/K_{\text{sp}}$ where a_i denotes the activity of the 366
 i^{th} species, and K_{sp} is the solubility product constant. The 367
 saturation index depends on pH, being lower at alkaline and 368
 higher at basic conditions.⁵¹ The precipitation of CC inside the 369
 channel started after an induction time of $t \sim 90$ min into the 370
 first hydrostatic phase. This was the time needed for the water 371
 in the channel to reach oversaturation and for the particles to 372
 grow to a detectable size. A similar delay in precipitation was 373
 predicted by the geochemical numerical model (SI S5). While 374
 CC did not precipitate in the channel during the induction 375
 time, a slight growth of the carbonation zone was observed. 376

377 When oversaturation was reached in the channel, the
378 carbonated zone stopped growing and CC precipitated in
379 the channel until the end of the first hydrostatic stage. The
380 precipitation started near the inlet where oversaturation was
381 first reached. The precipitation stopped and dissolution of CC
382 in the channel started right after the flow of CO_2 -saturated
383 water was introduced (Figure 4b). At the high flow rate used in
384 our experiment (1 mL/h, cf. Figure 1), the calculated
385 saturation index of calcite in the carbonated water is well
386 below 1 (Figure 3c). In such a significantly undersaturated
387 solution, CC dissolved continuously.

388 During the second hydrostatic stage, which lasted for 250
389 min, CC did not precipitate in the channel, in stark contrast to
390 the first hydrostatic stage. Still, the carbonated zone grew, and
391 the porous zone slightly shrank, which suggests that CC
392 precipitated preferentially inside the cement matrix rather than
393 in the channel. To understand why CC precipitated in the
394 channel during the first, but not the second hydrostatic phase,
395 we consider the changes that the cement system underwent
396 during the flow phase: (1) The carbonation front shifted ~ 0.4
397 mm further into the bulk, so the source of calcium was farther
398 away from the channel; (2) the porous silica zone grew larger,
399 and thus the volume in which oversaturation is needed to
400 induce precipitation has significantly increased (i.e., volume of
401 the channel plus the volume of pore spaces); (3) CC
402 precipitate was present in the channel. These changes increase
403 the induction time required to achieve oversaturation of
404 calcium and hydroxide ions, implying that CC could have
405 started to precipitate if the second hydrostatic stage had lasted
406 longer. The preferential precipitation inside the cement matrix
407 suggests that, within the duration of the second hydrostatic
408 phase, oversaturation was reached in the cement matrix only.
409 When the flow rate was increased to 1 mL/h, the remaining
410 CC in the channel started to dissolve. The dissolution rate
411 during the second flow phase was almost identical to that in
412 the first phase. The dissolution rate depends on the pH and
413 saturation index in the channel, which is similar in both
414 convective phases (Figure 3). The final increase in flow rate
415 from 1 to 20 mL/h consistently produced an even faster
416 dissolution of the remaining CC precipitate. A schematic
417 overview of the chemical processes in the sample during the
418 different stages of the CO_2 exposure is depicted in Figure 5,
419 highlighting that the CC precipitation or dissolution in the
420 channel when exposed to carbonated water depends on the
421 flow history: in the first period of flow, precipitation was
422 observed and in the second period of flow, no precipitation was
423 observed.

424 **Precipitation of CaCO_3 in the Fracture.** A 3D
425 visualization of the irregular “natural” fracture extending
426 vertically throughout the cement sample at $t = 0$ and $t =$
427 1200 min is displayed in Figure 4, and a series of μ -CT cross-
428 sections of the fracture at different stages are shown in Figure 1
429 and S11. The natural fracture was almost fully closed from the
430 beginning of the experiment, presumably due to the applied
431 confinement stress, leaving only a few small cavities open.
432 Although the fracture extended through the whole cement
433 sample, only regions of the fracture near the top of the sample
434 were filled by CC deposits (Figure S16). CC precipitation at
435 the upper surface of the fracture, i.e., “self-sealing”, likely
436 prevented the liquid flow from carbonating the fracture deeper
437 inside the cement.

438 However, CC precipitation occurred in the individual
439 fracture cavities when the diffusing CO_2 front emanating

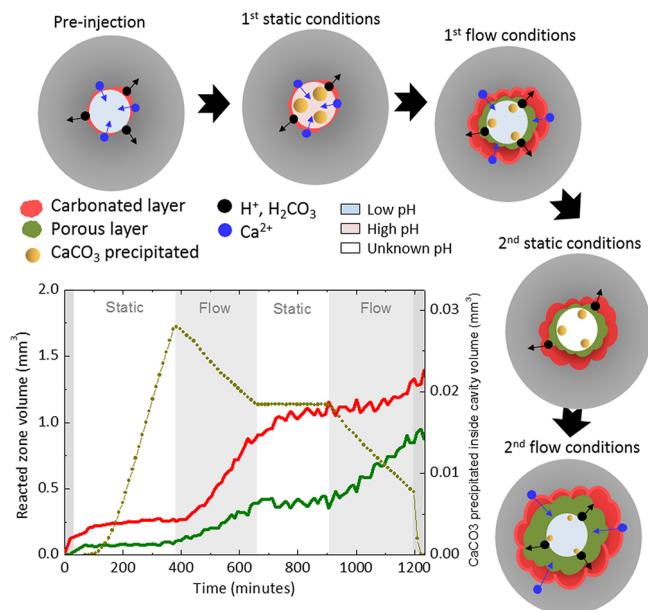


Figure 5. Schematic overview of the carbonation and self-sealing process of the sample during different stages of the CO_2 exposure.

440 from the nearby channel reached them, cf. Figure 1c. Detailed
441 analysis of the volume reduction due to the carbonation
442 process for a chosen single cavity is depicted in Figure 4c. This
443 specific cavity had a length and height of $\sim 300 \mu\text{m}$ and a width
444 of $\sim 100 \mu\text{m}$. Time-resolved volume filling of the very same
445 cavity as depicted in Figure 1c is shown in Figure 4c. During
446 the experiment, the cavity volume decreased by about 80%,
447 mainly due to the precipitation of CC . The μ -CT image
448 analysis shows that the precipitation in this selected cavity took
449 place after ~ 500 min. (Figure S13). The time anticipated for
450 self-sealing of a given cavity will depend on its position with
451 respect to the CO_2 exposed surfaces.

452 While the CC crystals precipitated in the channel were
453 isolated and localized, the precipitates in the fracture formed a
454 continuous lining along the surfaces of the fracture. The CC
455 layer was deposited not only at the side where the progressing
456 carbonation front first reached the fracture but evenly on all
457 the fracture surfaces, filling almost the entire original volume of
458 the fracture with CC (Figure S11). The difference in
459 appearance of the CC precipitate in the fracture (continuous
460 layer) and in the channel (discrete particles) may arise from
461 Ca^{2+} concentration, degree of saturation, pH, and surface
462 roughness. Intuitively, the concentration of Ca^{2+} in the isolated
463 fracture will be higher compared to the channel through which
464 fluid flow was forced. Typically, for high degrees of
465 oversaturation, CC nucleation may proceed so fast that most
466 dissolved material is used to constitute the nuclei, whereas little
467 is available for crystal growth. On the contrary, for low values
468 of oversaturation, nucleation may proceed slowly as most
469 dissolved material is consumed by crystal growth.⁵² Because of
470 the small size and isolated conditions of the fracture, the pH
471 inside the fracture is expected to be higher than in the channel;
472 therefore, oversaturation may be reached at lower calcium
473 concentrations. Indeed, it has been reported that at pH ~ 12 ,
474 smaller crystals form compared to those at pH 9.^{53,54} It is likely
475 that the polymorphic form of the CC precipitate will also be
476 affected by the different conditions in the fracture and the
477 cavity, which in turn may contribute to a different morphology
478 of the precipitate. The differences in surface morphology 478

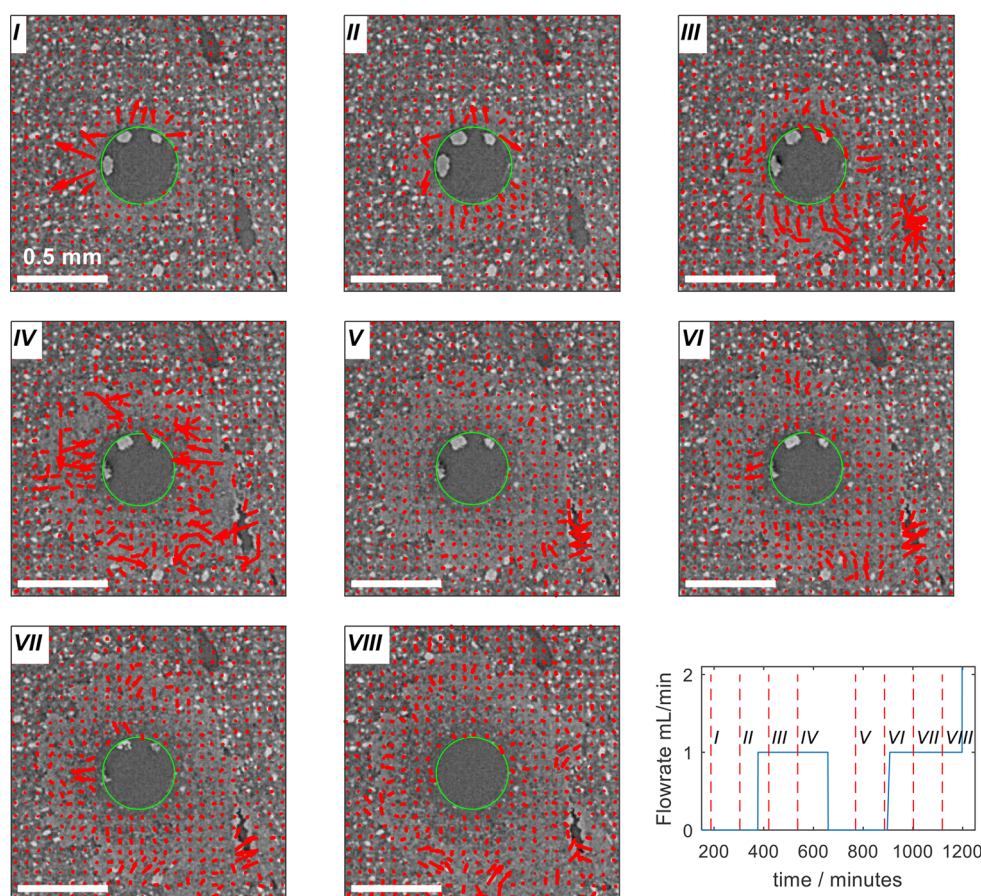


Figure 6. Time-resolved lateral distortions of the cement sample followed by DVC, near $z = 2$ mm. The displacement fields show the difference between μ -CT scans at the end and beginning of each interval, as indicated with Roman numerals. Note that essentially no changes are seen far from the channel, which is highlighted by a green circle. Stages I, II: Lateral expansion is observed from the start of the experiment near the artificial channel. Stage III: The carbonation front has reached the natural fracture in the down-right corner, which for the remainder of the experiment is seen to be monotonically squeezed. Stage IV exhibits high activity protruding further into the cement bulk, consistent with the liquid flow, while stage V (no-flow) only has small changes around the fracture. In stages VI–VII, the most notable observation is how the reaction has moved farther into the cement, leaving the surroundings of the channel effectively static. The magnitude of the displacement vectors is given in units of voxels multiplied by a factor 100, emphasizing that the distortions observed are indeed small.

479 between the smooth channel and the rough fracture might also
 480 have contributed to the qualitative differences in \overline{CC}
 481 precipitate appearance. For rough surfaces, it is proposed
 482 that protrusions act as nucleation sites.⁵⁵ In addition, a
 483 roughness of ~ 20 μm is reported to increase the surface
 484 wettability, which is a parameter directly related with the rate
 485 of nucleation.⁵⁶ The difference of the solute concentration in
 486 the aqueous bulk and the concentration close to the crystal
 487 surface is higher in the channel, and that promotes the creation
 488 of bigger crystals.⁵² As mentioned, the \overline{CC} precipitate appeared
 489 as a smooth lining of the whole fracture surfaces and not only
 490 on the carbonated side where the carbonation front first
 491 reached the fracture. In fact, the growth rate of the \overline{CC} layer
 492 was the same at the side facing the carbonation front as that at
 493 the side facing the nonreacted cement, suggesting that the
 494 oversaturation was relatively uniform across the fracture
 495 region.

496 **Geomechanical Analysis.** Digital volume correlation
 497 (DVC) was used to search for structural responses to the
 498 chemical reactions taking place within the sample. The 3D
 499 displacement field of the whole sample is fully consistent with
 500 the external triaxial stress state, revealing an expected axial
 501 compression, cf. SI. Subsequently, we focused on a comparably

502 small region near the channel within the sample, followed
 503 during eight distinct time intervals; see Figure 6. The fact that
 504 the specimen tilted slightly during the experiment necessitated
 505 the subtraction of the mean lateral displacement (effectively a
 506 sample translation at the small lengths scales of the investigated
 507 DVC volume) to reveal the finer details of the displacement
 508 field. Note that near the borders of the chosen DVC volume,
 509 i.e., far from the channel, essentially no changes are seen in any
 510 of the time intervals.

511 The DVC analysis indicates that local morphological
 512 changes were observed from the beginning of the experiment
 513 in the immediate surroundings of the channel, progressively
 514 protruding radially outward together with the carbonation
 515 front during the experiment (Figure 6). The deformation
 516 pattern surrounding the channel is understood to be induced
 517 by the local chemical alterations. During the time intervals of
 518 stagnant flow (particularly stage V), there is hardly any change
 519 to be seen around the channel.

520 The DVC analysis of the natural fractures observed in Figure
 521 6 (lower right corner) supports the preceding discussion,
 522 highlighting that once the reaction front has reached the
 523 fracture, the fracture starts closing. Note that in the same figure
 524 (upper right corner), there is also another cavity of the natural

525 fracture, which is never reached by the carbonation front and
526 consistently stays stationary throughout the experiment.

527 The observed changes seen by DVC may be explained by
528 several possible mechanisms which require further inves-
529 tigations. The DVC technique calculates the incremental
530 displacement components in the sample as macroscopic
531 deformation progresses.⁴⁰ However, local modifications of
532 the X-ray absorption properties due to chemical reaction may
533 introduce a bias on the calculation of the incremental strain in
534 the sample. Consequently, DVC allows the detection of
535 locations with significant strain and/or chemical reaction, but a
536 quantitative separation between these two components cannot
537 readily be achieved. Because the bulk regions of the specimen
538 are not reached by the carbonation front, we expect the DVC
539 results in the bulk regions (see Figure S17) to stem from
540 genuine mechanical deformations. Conversely, the region
541 shown in Figure 6 is close to the channel, and the DVC
542 changes are strongly correlated with the carbonation front,
543 suggesting that a significant part of the signal picked up by the
544 DVC analysis is caused by chemical reactions rather than
545 mechanical displacement.

546 To the extent mechanical distortion is present, at least two
547 mechanisms can be envisioned. First, the decrease of porosity
548 in the carbonated zone^{57,58} may induce a local increase of the
549 elastic modulus due to phase transformation.⁵⁰ The cement
550 becomes stronger macroscopically with carbonation while a
551 reorganization of the microstructure takes place at small
552 scale.⁵⁹ Second, by the force of crystallization,⁶⁰ a reorganiza-
553 tion of the microstructure can be triggered by the stress caused
554 by volume expansion of the carbonated cement, since
555 carbonation of portlandite results in a net increase of volume.⁶⁰
556 Independent of the exact mechanism, intensity correlation-
557 based DVC is evidently a powerful tool for quantitatively
558 exploring minor structural changes inside the specimen.

559 **Environmental Implications.** Our study presents un-
560 precedented time-lapse 3D imaging of the progressive
561 degradation of Portland cement and the concomitant
562 precipitation and dissolution of CaCO₃ in leakage pathways
563 with exposure to sc-CO₂. Importantly, the data was obtained in
564 situ, showing the response to carbonated water at controlled
565 flow rates under realistic reservoir conditions of high pressure
566 and temperature. The alternated application of stagnant and
567 flow-through conditions during the experiment aided delin-
568 eation of precipitation versus dissolution-dominated regimes:
569 information that can only be achieved through in situ
570 laboratory experiments and potentially can be used for solving
571 imminent environmental challenges related to CO₂ storage.
572 The methodology of increasingly realistic in situ imaging
573 experiments combined with advanced modeling is destined to
574 find many applications in the environmental and material
575 sciences in the coming years. In the present study, experiments
576 and geochemical modeling confirm that conditions with small
577 CO₂ flow rates promote the formation of the carbonated zone
578 and subsequently precipitation of CaCO₃ in large cavities.
579 Conversely, in a leakage path with a comparably high CO₂ flow
580 rate, the formation of a weak and porous silica layer can
581 severely degrade the cement. An important new finding relying
582 on the in situ approach is the demonstration that the CO₂
583 leakage risk from a well bore is severely impacted not only by
584 the flow conditions but also by the flow history.

■ ASSOCIATED CONTENT

Supporting Information

The Supporting Information is available free of charge at
<https://pubs.acs.org/doi/10.1021/acs.est.0c00578>.

Information regarding sample preparation, experimental
details, X-ray attenuation of cement phases, image
processing, portlandite depleted zone, chemical numer-
ical model, μ -CT cross-section images of cement
without color segmentation, additional volume calcu-
lations of the reacted zones in the cement, and
mechanical response in the cement (PDF)
Movie showing cross-section slice at the middle of the
sample during the CO₂ exposure (AVI)
Movie showing the 3D visualization of precipitated
CaCO₃ in the channel during the CO₂ exposure (The
reconstructed tomograms are available from the
corresponding author upon request.) (AVI)

■ AUTHOR INFORMATION

Corresponding Authors

Elvia A. Chavez Panduro – Department of Physics, Norwegian
University of Science and Technology (NTNU), 7491
Trondheim, Norway; SINTEF Energy Research, NO-7465
Trondheim, Norway; orcid.org/0000-0003-3732-356X;
Email: elviachavezp@gmail.com

Dag W. Breiby – PoreLab, Department of Physics, Norwegian
University of Science and Technology (NTNU), 7491
Trondheim, Norway; Department of Microsystems, University of
South-Eastern Norway, 3184 Borre, Norway;
Email: dag.breiby@ntnu.no

Authors

Benoît Cordonnier – The Njord Centre, Department of
Geosciences, University of Oslo, Oslo 0315, Norway; ESRF,
European Synchrotron Radiation Facility, 38000 Grenoble,
France

Kamila Gawel – SINTEF Industry, 7031 Trondheim, Norway
Ingrid Børve – Department of Physics, Norwegian University of
Science and Technology (NTNU), 7491 Trondheim, Norway

Jaisree Iyer – Atmospheric Earth and Energy Division, Lawrence
Livermore National Laboratory, Livermore, California 94550,
United States; orcid.org/0000-0002-1154-3030

Susan A. Carroll – Atmospheric Earth and Energy Division,
Lawrence Livermore National Laboratory, Livermore,
California 94550, United States; orcid.org/0000-0002-6456-3318

Leander Michels – Department of Physics, Norwegian
University of Science and Technology (NTNU), 7491
Trondheim, Norway; orcid.org/0000-0002-0023-681X

Melania Rogowska – Department of Chemistry, University of
Copenhagen, 2100 Copenhagen Ø, Denmark

Jessica Ann McBeck – The Njord Centre, Department of
Geosciences, University of Oslo, Oslo 0315, Norway

Henning Osholm Sørensen – Department of Chemistry,
University of Copenhagen, 2100 Copenhagen Ø, Denmark;
Department of Physics, Technical University of Denmark, 2800
Kongens Lyngby, Denmark; orcid.org/0000-0002-7004-547X

Stuart D. C. Walsh – Resources Engineering, Monash University,
Melbourne, VIC 3800, Australia

François Renard – The Njord Centre, Department of
Geosciences, University of Oslo, Oslo 0315, Norway; University

645 Grenoble Alpes, University Savoie Mont Blanc, CNRS, IRD,
646 IFSTTAR, ISTerre, 38000 Grenoble, France; [orcid.org/](https://orcid.org/0000-0002-5125-5930)
647 0000-0002-5125-5930
648 Alain Gibaud – LUNAM, IMMM, UMR 6283 CNRS, Le
649 Mans Université, 72085 Le Mans Cedex 09, France
650 Malin Torsæter – SINTEF Industry, 7031 Trondheim, Norway

651 Complete contact information is available at:
652 <https://pubs.acs.org/10.1021/acs.est.0c00578>

653 Author Contributions

654 The experiment was planned and coordinated by A.G.,
655 E.A.C.P., M.T. and D.W.B. The sample cell was designed by
656 F.R. and B.C. and constructed by Sanchez Technologies. The
657 experiment at the synchrotron was carried out by B.C., L.M.,
658 M.R., H.O.S., and A.G., while the data analysis was done by
659 E.A.C.P., I.B., K.G., and D.W.B. The geochemical modeling was
660 done by J.I., S.D.C.W., and S.C. The mechanical analysis was
661 performed by B.C., J.A.M., F.R., and D.W.B., E.A.C.P., K.G.,
662 and D.W.B. wrote the article. All authors have read and
663 approved the final version of the manuscript.

664 Notes

665 The authors declare no competing financial interest.

666 ■ ACKNOWLEDGMENTS

667 Elodie Boller at the European Synchrotron Radiation Facility
668 (ESRF) in Grenoble, France, is thanked for technical support.
669 This study received funding from the Norwegian Research
670 Council (projects: CO₂PLUG, grant 243765; Prometheus,
671 grant 267775; and COMPMIC, 275182) and beam time was
672 allocated at the ESRF. Data storage was provided by
673 UNINETT Sigma2 - the National Infrastructure for High
674 Performance Computing and Data Storage in Norway (project
675 NS9073K). J.I. and S.C. from Lawrence Livermore National
676 Laboratory performed the work under the Contract DE-AC52-
677 07NA27344. H.O.S. received funding for travelling to the
678 synchrotron facility from the Danish Agency for Science,
679 Technology and Innovation via Danscatt. DWB thanks the
680 Research Council of Norway for funding its Centres of
681 Excellence funding scheme, project number 262644, Centre for
682 Porous Media Laboratory.

683 ■ REFERENCES

684 (1) IPCC, 2007: *Climate Change 2007: The Physical Science Basis*; p
685 996.
686 (2) IPCC, 2005: *IPCC Special Report on Carbon Dioxide Capture and*
687 *Storage*; p 442.
688 (3) Viswanathan, H. S.; Pawar, R. J.; Stauffer, P. H.; Kaszuba, J. P.;
689 Carey, J. W.; Olsen, S. C.; Keating, G. N.; Kavetski, D.; Guthrie, G. D.
690 Development of a hybrid process and system model for the
691 assessment of wellbore leakage at a geologic CO₂ sequestration site.
692 *Environ. Sci. Technol.* **2008**, *42* (19), 7280–6.
693 (4) Kutchko, B.; Strazisar, B. R.; Dzombak, D. A.; Lowry, G. V.;
694 Thaulow, N. Degradation of Well Cement by CO₂ under Geologic
695 Sequestration Conditions. *Environ. Sci. Technol.* **2007**, *41* (13), 13.
696 (5) Mason, H. E.; Du Frane, W. L.; Walsh, S. D.; Dai, Z.;
697 Charnvanichborikarn, S.; Carroll, S. A. Chemical and mechanical
698 properties of wellbore cement altered by CO₂-rich brine using a
699 multianalytical approach. *Environ. Sci. Technol.* **2013**, *47* (3), 1745–
700 52.
701 (6) Huerta, N. J.; Hesse, M. A.; Bryant, S. L.; Strazisar, B. R.;
702 Lopano, C. Reactive transport of CO₂-saturated water in a cement
703 fracture: Application to wellbore leakage during geologic CO₂ storage.
704 *Int. J. Greenhouse Gas Control* **2016**, *44*, 276–289.

(7) Kutchko, B. G.; Strazisar, B. R.; Huerta, N.; Lowry, G. V.; 705
Dzombak, D. A.; Thaulow, N. CO₂ Reaction with Hydrated Class H 706
Well Cement under Geologic Sequestration Conditions: Effects of 707
Flyash Admixtures. *Environ. Sci. Technol.* **2009**, *43*, 3947–3952. 708
(8) Rimmelé, G.; Barlet-Gouédard, V.; Porcherie, O.; Goffé, B.; 709
Brunet, F. Heterogeneous porosity distribution in Portland cement 710
exposed to CO₂-rich fluids. *Cem. Concr. Res.* **2008**, *38* (8–9), 1038– 711
1048. 712
(9) Duguid, A.; Scherer, G. W. Degradation of oilwell cement due to 713
exposure to carbonated brine. *Int. J. Greenhouse Gas Control* **2010**, *4* 714
(3), 546–560. 715
(10) Luquot, L.; Abdoulghafour, H.; Gouze, P. Hydro-dynamically 716
controlled alteration of fractured Portland cements flowed by CO₂- 717
rich brine. *Int. J. Greenhouse Gas Control* **2013**, *16*, 167–179. 718
(11) Mason, H. E.; Walsh, S. D.; DuFrane, W. L.; Carroll, S. A. 719
Determination of diffusion profiles in altered wellbore cement using 720
X-ray computed tomography methods. *Environ. Sci. Technol.* **2014**, *48* 721
(12), 7094–100. 722
(12) Cao, P.; Karpyn, Z. T.; Li, L. Self-healing of cement fractures 723
under dynamic flow of CO₂-rich brine. *Water Resour. Res.* **2015**, *51* 724
(6), 4684–4701. 725
(13) Carroll, S.; Carey, J. W.; Dzombak, D.; Huerta, N. J.; Li, L.; 726
Richard, T.; Um, W.; Walsh, S. D. C.; Zhang, L. Review: Role of 727
chemistry, mechanics, and transport on well integrity in CO₂ storage 728
environments. *Int. J. Greenhouse Gas Control* **2016**, *49*, 149–160. 729
(14) Kutchko, B. G.; Strazisar, B. R.; Lowry, G. V.; Dzombak, D. A.; 730
Thaulow, N. Rate of CO₂ attack on hydrated Class H well cement 731
under geologic sequestration conditions. *Environ. Sci. Technol.* **2008**, 732
42 (16), 6237–42. 733
(15) Brunet, J.-P. L.; Li, L.; Karpyn, Z. T.; Kutchko, B. G.; Strazisar, 734
B.; Bromhal, G. Dynamic Evolution of Cement Composition and 735
Transport Properties under Conditions Relevant to Geological 736
Carbon Sequestration. *Energy Fuels* **2013**, *27* (8), 4208–4220. 737
(16) Walsh, S. D. C.; Du Frane, W. L.; Mason, H. E.; Carroll, S. A. 738
Permeability of Wellbore-Cement Fractures Following Degradation 739
by Carbonated Brine. *Rock Mechanics and Rock Engineering* **2013**, *46* 740
(3), 455–464. 741
(17) Liteanu, E.; Spiers, C. J. Fracture healing and transport 742
properties of wellbore cement in the presence of supercritical CO₂. 743
Chem. Geol. **2011**, *281* (3–4), 195–210. 744
(18) Matteo, E. N.; Huet, B.; Jové-Colón, C. F.; Scherer, G. W. 745
Experimental and modeling study of calcium carbonate precipitation 746
and its effects on the degradation of oil well cement during 747
carbonated brine exposure. *Cem. Concr. Res.* **2018**, *113*, 1–12. 748
(19) Iyer, J.; Walsh, S. D. C.; Hao, Y.; Carroll, S. A. Incorporating 749
reaction-rate dependence in reaction-front models of wellbore- 750
cement/carbonated-brine systems. *Int. J. Greenhouse Gas Control* 751
2017, *59*, 160–171. 752
(20) Cao, P.; Karpyn, Z. T.; Li, L. Dynamic alterations in wellbore 753
cement integrity due to geochemical reactions in CO₂-rich environ- 754
ments. *Water Resour. Res.* **2013**, *49* (7), 4465–4475. 755
(21) Wigand, M.; Kaszuba, J. P.; Carey, J. W.; Hollis, W. K. 756
Geochemical effects of CO₂ sequestration on fractured wellbore 757
cement at the cement/caprock interface. *Chem. Geol.* **2009**, *265* (1– 758
2), 122–133. 759
(22) Guthrie, G. D.; Pawar, R. J.; Carey, J. W.; Karra, S.; Harp, D. R.; 760
Viswanathan, H. S. The mechanisms, dynamics, and implications of 761
self-sealing and CO₂ resistance in wellbore cements. *Int. J. Greenhouse* 762
Gas Control **2018**, *75*, 162–179. 763
(23) Brunet, J.-P. L.; Li, L.; Karpyn, Z. T.; Huerta, N. J. Fracture 764
opening or self-sealing: Critical residence time as a unifying parameter 765
for cement–CO₂–brine interactions. *Int. J. Greenhouse Gas Control* 766
2016, *47*, 25–37. 767
(24) Newell, D. L.; Carey, J. W. Experimental evaluation of wellbore 768
integrity along the cement-rock boundary. *Environ. Sci. Technol.* **2013**, 769
47 (1), 276–82. 770
(25) Um, W.; Jung, H.; Kabilan, S.; Suh, D.; Fernandez, C. 771
Geochemical and Geomechanical Effects on Wellbore Cement Fractures: 772

- 773 *Data Information for Wellbore Reduced Order Mode*; Pacific Northwest
774 National Laboratory Richland: WA, January, 2014.
- 775 (26) Wolterbeek, T. K. T.; Peach, C. J.; Raouf, A.; Spiers, C. J.
776 Reactive transport of CO₂-rich fluids in simulated wellbore interfaces:
777 Flow-through experiments on the 1–6 m length scale. *Int. J.*
778 *Greenhouse Gas Control* **2016**, *54*, 96–116.
- 779 (27) Wolterbeek, T. K. T.; Ruckert, F.; van Moorsel, S. G.;
780 Cornelissen, E. K. Reactive transport and permeability evolution in
781 wellbore defects exposed to periodic pulses of CO₂-rich water. *Int. J.*
782 *Greenhouse Gas Control* **2019**, *91*, 102835.
- 783 (28) Han, W. S.; Lu, M.; McPherson, B. J.; Keating, E. H.; Moore, J.;
784 Park, E.; Watson, Z. T.; Jung, N. H. Characteristics of CO₂-driven
785 cold-water geyser, Crystal Geyser in Utah: experimental observation
786 and mechanism analyses. *Geofluids* **2013**, *13* (3), 283–297.
- 787 (29) Jung, H. B.; Kabilan, S.; Carson, J. P.; Kuprat, A. P.; Um, W.;
788 Martin, P.; Dahl, M.; Kafentzis, T.; Varga, T.; Stephens, S.; Arey, B.;
789 Carroll, K. C.; Bonneville, A.; Fernandez, C. A. Wellbore cement
790 fracture evolution at the cement–basalt caprock interface during
791 geologic carbon sequestration. *Appl. Geochem.* **2014**, *47*, 1–16.
- 792 (30) Kampman, N.; Burnside, N. M.; Shipton, Z. K.; Chapman, H.
793 J.; Nicholl, J. A.; Ellam, R. M.; Bickle, M. J. Pulses of carbon dioxide
794 emissions from intracrustal faults following climatic warming. *Nat.*
795 *Geosci.* **2012**, *5* (5), 352–358.
- 796 (31) Watson, T. L. *Surface Casing Vent Flow Repair—A Process*. In
797 *Petroleum Society's 5th Canadian International Petroleum Conference*
798 *(55th Annual Technical Meeting)*, Calgary, Alberta, Canada, 2004.
- 799 (32) Carey, J. W.; Wigand, M.; Chipera, S. J.; WoldeGabriel, G.;
800 Pawar, R.; Lichtner, P. C.; Wehner, S. C.; Raines, M. A.; Guthrie, G.
801 D. Analysis and performance of oil well cement with 30 years of CO₂
802 exposure from the SACROC Unit, West Texas, USA. *Int. J.*
803 *Greenhouse Gas Control* **2007**, *1* (1), 75–85.
- 804 (33) Crow, W.; Carey, J. W.; Gasda, S.; Brian Williams, D.; Celia, M.
805 Wellbore integrity analysis of a natural CO₂ producer. *Int. J.*
806 *Greenhouse Gas Control* **2010**, *4* (2), 186–197.
- 807 (34) Chavez Panduro, E. A.; Torsæter, M.; Gawel, K.; Bjorge, R.;
808 Gibaud, A.; Yang, Y.; Bruns, S.; Zheng, Y.; Sorensen, H. O.; Breiby, D.
809 W. In-Situ X-ray Tomography Study of Cement Exposed to CO₂
810 Saturated Brine. *Environ. Sci. Technol.* **2017**, *51* (16), 9344–9351.
- 811 (35) Renard, F.; Cordonnier, B.; Dysthe, D. K.; Boller, E.; Tafforeau,
812 P.; Rack, A. A deformation rig for synchrotron microtomography
813 studies of geomaterials under conditions down to 10 km depth in the
814 Earth. *J. Synchrotron Radiat.* **2016**, *23* (4), 1030.
- 815 (36) Standard 10 B-2. (API), American Petroleum Institute.
- 816 (37) Paganin, D.; Mayo, S. C.; Gureyev, T. E.; Miller, P. R.; Wilkins,
817 S. W. Simultaneous phase and amplitude extraction from a single
818 defocused image of a homogeneous object. *J. Microsc.* **2002**, *206* (1),
819 33–40.
- 820 (38) Mirone, A.; Brun, E.; Gouillart, E.; Tafforeau, P.; Kieffer, J. The
821 PyHST2 hybrid distributed code for high speed tomographic
822 reconstruction with iterative reconstruction and a priori knowledge
823 capabilities. *Nucl. Instrum. Methods Phys. Res., Sect. B* **2014**, *324*, 41–
824 48.
- 825 (39) Walsh, S. D. C.; Mason, H. E.; Du Frane, W. L.; Carroll, S. A.
826 Experimental calibration of a numerical model describing the
827 alteration of cement/caprock interfaces by carbonated brine. *Int. J.*
828 *Greenhouse Gas Control* **2014**, *22*, 176–188.
- 829 (40) Tudisco, E.; Andò, E.; Cailletaud, R.; Hall, S. A. TomoWarp2:
830 A local digital volume correlation code. *SoftwareX* **2017**, *6*, 267–270.
- 831 (41) McBeck, J. A.; Cordonnier, B.; Vinciguerra, S.; Renard, F.
832 Volumetric and Shear Strain Localization in Mt. Etna Basalt. *Geophys.*
833 *Res. Lett.* **2019**, *46* (5), 2425–2433.
- 834 (42) McBeck, J. A.; Kobchenko, M.; Hall, S. A.; Tudisco, E.;
835 Cordonnier, B.; Meakin, P.; Renard, F. Investigating the Onset of
836 Strain Localization Within Anisotropic Shale Using Digital Volume
837 Correlation of Time-Resolved X-Ray Microtomography Images.
838 *Journal of Geophysical Research Solid Earth* **2018**, *123* (9), 7509–7528.
- 839 (43) Study of High Pressure High Temperature Zones in the Gulf of
840 Mexico; 2017.
- (44) Duguid, A.; Radonjic, M.; Scherer, G. W. *Degradation of Well*
841 *Cements Exposed to Carbonated Brine*. In Fourth Annual Conference
842 on Carbon Capture and Sequestration Doinetel, 2005. 843
- (45) Abdoulghafour, H.; Luquot, L.; Gouze, P. Characterization of
844 the mechanisms controlling the permeability changes of fractured
845 cements flowed through by CO₂-rich brine. *Environ. Sci. Technol.*
846 **2013**, *47* (18), 10332–8. 847
- (46) Panduro, E. A. C.; Torsæter, M.; Gawel, K.; Bjørge, R.; Gibaud,
848 A.; Yang, Y.; Sørensen, H. O.; Frykmanf, P.; Kjøllef, C.; Breiby, D. W.
849 *Closing of micro-cavities in well cement upon exposure to CO₂ brine*. In
850 *13th International Conference on Greenhouse Gas Control Technologies*,
851 *GHGT-13*, Lausanne, Switzerland, 2016. 852
- (47) Chavez Panduro, E. A.; Torsæter, M.; Gawel, K.; Bjørge, R.;
853 Gibaud, A.; Bonnin, A.; Schlepütz, C. M.; Breiby, D. W. Computed X-
854 ray Tomography Study of Carbonate Precipitation in Large Portland
855 Cement Pores. *Cryst. Growth Des.* **2019**, *19* (10), 5850–5857. 856
- (48) Andreassen, J.-P. Formation mechanism and morphology in
857 precipitation of vaterite—nano-aggregation or crystal growth? *J. Cryst.*
858 *Growth* **2005**, *274* (1–2), 256–264. 859
- (49) Beuvier, T.; Calvignac, B.; Delcroix, G. J.-R.; Tran, M. K.;
860 Kodjikian, S.; Delorme, N.; Bardeau, J.-F.; Gibaud, A.; Boury, F. 861
862 Synthesis of hollow vaterite CaCO₃ microspheres in supercritical
863 carbon dioxide medium. *J. Mater. Chem.* **2011**, *21*, 9757–9761. 863
- (50) Oral, Ç. M.; Ercan, B. Influence of pH on morphology, size and
864 polymorph of room temperature synthesized calcium carbonate
865 particles. *Powder Technol.* **2018**, *339*, 781–788. 866
- (51) de Moel, P. J.; van der Helm, A. W. C.; van Rijn, M.; van Dijk,
867 J. C.; van der Meer, W. G. J. Assessment of calculation methods for
868 calcium carbonate saturation in drinking water for DIN 38404–10
869 compliance. *Drinking Water Eng. Sci.* **2013**, *6* (2), 115–124. 870
- (52) Luigi, M. *Geological Sequestration of Carbon Dioxide: 871*
872 *Thermodynamics, Kinetics, and Reaction Path Modeling*. 1st ed.;
873 Elsevier: 2007. 873
- (53) Yu, J.; Lei, M.; Cheng, B.; Zhao, X. Effects of PAA additive and
874 temperature on morphology of calcium carbonate particles. *J. Solid*
875 *State Chem.* **2004**, *177* (3), 681–689. 876
- (54) Declat, A.; Reyes, E.; Suarez, M. Calcium Carbonate
877 Precipitation: A Review of the Carbonate Crystallization Process
878 and Applications in Bioinspired Composites. *Review on Advanced*
879 *Materials Science* **2016**, *44*, 87–107. 880
- (55) Bohnet, M. Influence of the transport properties of the crystal/
881 heat transfer surface interfacial on fouling behavior. *Chem. Eng.*
882 *Technol.* **2003**, *26* (10), 1055–1060. 883
- (56) Keysar, S.; Semiat, R.; Hasson, D.; Yahalom, J. Effect of Surface
884 Roughness on the Morphology of Calcite Crystallizing on Mild Steel.
885 *J. Colloid Interface Sci.* **1994**, *162*, 311–319. 886
- (57) Savija, B.; Luković, M. Carbonation of cement paste:
887 Understanding, challenges, and opportunities. *Construction and*
888 *Building Materials* **2016**, *117*, 285–301. 889
- (58) Johannesson, B.; Utgenannt, P. Microstructural changes caused
890 by carbonation of cement mortar. *Cem. Concr. Res.* **2001**, *31* (6),
891 925–931. 892
- (59) Lecampion, B.; Vanzo, J.; Ulm, F.; Huet, B.; Gernay, C.;
893 Khafallah, I. *Evolution of Portland cement mechanical properties exposed*
894 *to CO₂ rich fluids: investigation at different scales*. In *Mechanics and*
895 *Physics of Porous Solids (MPPS) – A tribute to Prof Olivier Coussy*,
896 Paris, France, 2011. 897
- (60) Wolterbeek, T. K. T. *Impact of chemical and mechanical processes*
898 *on wellbore integrity in CO₂ storage systems*. Utrecht University,
899 Utrecht, The Netherlands, 2016. 900